Journal of Power Sources 192 (2009) 414–422

Contents lists available at ScienceDirect

Journal of Power Sources

journal homepage: www.elsevier.com/locate/jpowsour

Effects of operating conditions on the performance of a micro-tubular solid oxide fuel cell (SOFC)

Mustafa Fazil Serincan[a,*], Ugur Pasaogullari[a], Nigel M. Sammes[b]

[a] Department of Mechanical Engineering, and Connecticut Global Fuel Cell Center, University of Connecticut, 44 Weaver Road Unit 5233, Storrs, CT, USA
[b] Department of Metallurgical and Materials Engineering, Colorado School of Mines, 1500 Illinois Street, Golden, CO, USA

ARTICLE INFO

Article history:
Received 5 March 2009
Received in revised form 24 March 2009
Accepted 24 March 2009
Available online 2 April 2009

Keywords:
SOFC
Micro-tubular
Leakage currents
Parametric analysis
CFD
Dusty gas model

ABSTRACT

A parametric analysis is carried out to study the effects of the operating conditions on the performance and operation of a micro-tubular solid oxide fuel cell. The computational fluid dynamics model incorporates mass, momentum, species and energy balances along with ionic and electronic charge transfers. Effects of temperature, fuel flow rate, fuel composition, anode pressure and cathode pressure on fuel cell performance are investigated. Polarization curves are compared to allow an understanding of the effects of different operating conditions on the performance of the fuel cell. Effects of anode flow rate on fuel cell efficiency and fuel utilization are also investigated. Moreover, influence of operating temperature on the internal electronic current leaks is outlined. Temperature distributions, current density profiles and hydrogen mole fraction profiles are also utilized to have a better understanding of the spatial effects of operating parameters. It is predicted that at 550 °C, for an output current demand of 0.53 A cm^{-2}, fuel cell needs to generate 0.65 A cm^{-2} ionic current density where the difference in these values is attributed to internal current leaks. On the other hand for temperatures lower than 500 °C, the effect of electronic leakage currents are not significant.

1. Introduction

As fossil fuel supplies become insufficient to match the increased energy demand, there is a steady increase in the search for alternative energy sources and utilizing technologies. In this context solid oxide fuel cells (SOFC) have been shown to be the promising candidates due to fuel flexibilities [1,2], and due to the high operating temperatures these systems are favorable for cogeneration applications to have an increase overall system efficiency with the utilization of the waste heat [3–5]. These systems are not commercially available yet due to high cost of the materials and lack of optimization of the fuel cell geometry and operation.

With the advances in computer technologies, more complex systems can be modeled and modeling has become a major alternative method to understand the fuel cell operation as well as to outline the factors affecting fuel cell performance. The modeling results can be utilized to suggest guidelines for optimization of the systems.

Although there are substantial studies in modeling of SOFCs [6–9], few modeling work has focused on the parametric analysis. Parametric analysis is an important method to understand the fuel cell behavior and compare the performance of the system affected by various factors. These factors can be related to either cell geometry, material properties or operation conditions. Changes in the geometry of the cell come along with the uncertainties in the parameters related to reaction kinetics as the latter cannot be predicted without additional experiments. If the fuel cell performance is desired to be compared for two different cathode thicknesses, parameters related to reaction kinetics have to be updated for the new geometry as the distribution of the three phase boundaries will change along with the percolation of the phases in the new geometry. Many of the modeling studies found in the literature carrying out parametric analyses of SOFCs focus on the geometrical aspects of the system [10–15]. However, these studies neglect the above-mentioned uncertainties arising with the change of the electrode geometry and are incapable of providing a precise tool to assess the effects of the geometrical parameters. Therefore in this study we do not focus on the effects of geometry on the fuel cell performance.

There are also studies focusing on the operational parameters such as utilization, flow rate, temperature and pressure [10,12,13,16–20]. Ni et al. [10–12] developed a model to conduct parametric analysis to address the effects of operating conditions on the overpotentials. Their work constitutes a 1D model employing electrochemical relations and mass balances, and does not include energy and momentum balances. Jiang et al. [13] built a thermal and electrochemical model of a tubular SOFC to study the effects of operating conditions such as pressure, temperature and flow rate.

* Corresponding author. Tel.: +1 860 949 3526; fax: +1 860 486 8378.
E-mail addresses: fazil.serincan@engr.uconn.edu (M.F. Serincan), ugurpasa@engr.uconn.edu (U. Pasaogullari), nsammes@mines.edu (N.M. Sammes).

0378-7753/$ – see front matter © 2009 Elsevier B.V. All rights reserved.
doi:10.1016/j.jpowsour.2009.03.049

Nomenclature

A	pre-exponential constant
C_p	specific heat
EA	electrode activation energy
F	Faraday constant
h	enthalpy
i	exchange current density
k	thermal conductivity
k_b	Boltzmann constant
K	permeability
M	molecular weight
n	number of species
p	pressure
Q	volumetric heat source
r	average pore radius
R	volumetric consumption
R	universal gas constant
T	temperature
$\mathbf{u}$	velocity vector
w	species mass fraction
x	species mole fraction

Greek letters

α	transfer coefficient
γ	concentration dependency
η	overpotential
ρ	density
σ	conductivity
τ	tortuosity
ϕ	potential
μ	dynamic viscosity
ε	porosity

Subscripts

a	anode
c	cathode
elc	electrolyte
j	species
k	species
i	ionic
e	electronic
eq	equilibrium
eff	effective
Kn	Knudsen

Superscripts

for	formation
in	inlet
reac	reacted
T	transpose
Th	thermal

Their model is a lumped model and does not consider spatial distributions of the variables. Lisbona et al. [16] analyzed a SOFC stack with the balance of plant to develop relations between cell performance and the operational parameters such as utilization, air flow rate and inlet gas temperature. The developed model consists of only electrochemical relations and the transport phenomena inside the stack are not considered. Colpan et al. [17] developed a model employing thermodynamic calculations to identify the effects of utilization on cell output power and efficiency. Bove et al. [18] carried out a utilization analysis for a tubular SOFC. Their model employs energy balance and electrochemical relations along with the simple algebraic relations for gas compositions. Although these models constitute significant contributions to the field, they either do not incorporate the sophisticated transport phenomena in the fuel cell rigorously or they underestimate the effects of spatial distributions of the transport variables.

In this paper, we present a parametric analysis of a micro-tubular SOFC with a model previously developed by us [21] to investigate the effects of operating parameters on the performance and operation. Due to the previously mentioned uncertainties related to changes in geometry and material properties, we only focus on the effects of the operating parameters such as temperature, fuel flow rate and composition, inlet humidity and back pressure of the anode. The model exploits the axial symmetry of the tubular geometry therefore reduces the modeling domain into a two-dimensional axisymmetric domain assuming the anode and the cathode current collectors is uniformly distributed on the electrode surfaces. The model solves for mass, species, momentum and energy conservation along with electrochemical kinetics and ionic and electronic charge conservation.

The properties for the cells that are modeled here are taken from the experimental micro-tubular cells that are fabricated and characterized by New Energy and Industrial Technology Development Organization (NEDO) of Japan [22]. The micro-tubular cells are composed of NiO–GDC anode, GDC electrolyte and $La_{0.8}Sr_{0.2}Co_{0.6}Fe_{0.4}O_3$ (LSCF)–GDC cathode. A common problem with ceria based electrolytes is that they can be reduced under fuel cell operating conditions, consequently becoming electronically conductive [23] resulting in electron transfer from anode to cathode through the electrolyte. As a result the cell is short circuited and a drop in open circuit voltage (OCV) is observed. We call this phenomenon as the "internal current leak", and the model is capable of capturing this behavior of the electrolyte due to the mixed ionic-electronic conductor (MIEC) behavior of the electrolyte.

2. Description of the mathematical model

The model domain is shown in Fig. 1. The actual three-dimensional geometry of the domain can be visualized by revolving the figure around the symmetry axis. The dimensions of the cell are provided in Table 1. The equations solved in the model are specified in each section in Fig. 1.

Momentum equation is solved with the continuity equation in the air and the fuel channels. In the electrodes, the momentum equation is modified by Darcy's law to model the transport in the porous media. Multi-component species conservation is modeled via Maxwell–Stefan equations in the open channels and the porous media. To account for porosity, diffusion coefficients are modified in the electrodes. Moreover, dusty gas model is implemented in the electrodes to take into account Knudsen diffusion due to comparable length scale of pores to the mean free path length of the gases. The energy equation is solved over the entire modeled domain. Conservation of charge is taken into consideration separately for both ionic and electronic charges. Ionic charge equations are solved in the

Table 1
Geometrical parameters.

Property	Value
Inner anode diameter	0.8 mm
Anode thickness	0.4 mm
Electrolyte thickness	30 μm
Cathode thickness	70 μm
Anode length	10 mm
Electrolyte length	10 mm
Cathode length	7 mm
Anode porosity (after reduction of NiO)	0.45
Cathode porosity	0.55

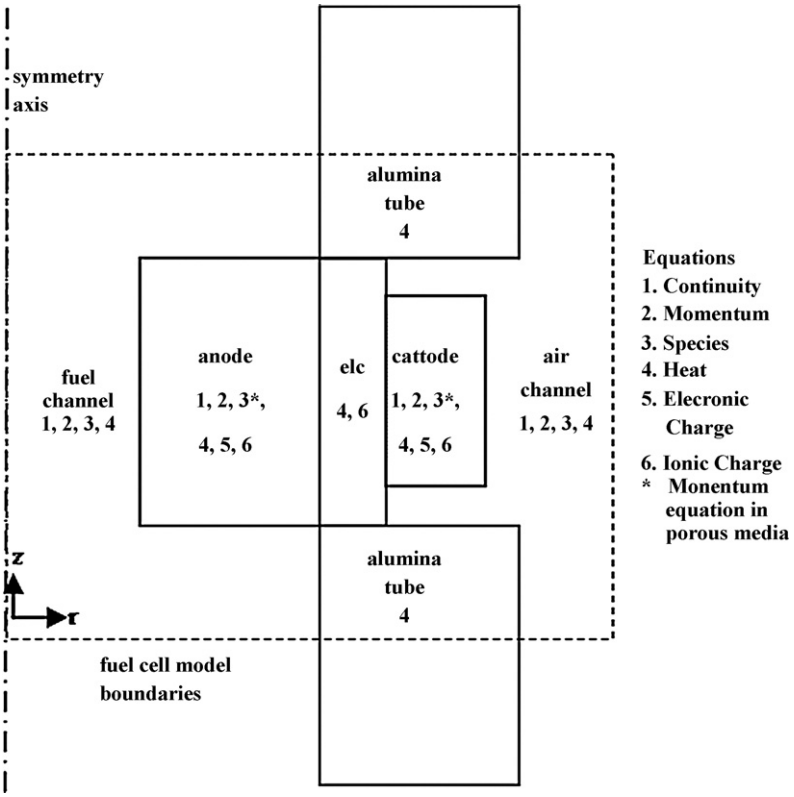

Fig. 1. Model geometry and the equations solved in the model.

Table 2
Governing equations.

Mass	$\nabla \cdot (\rho \mathbf{u}) = R_j$	(1)
Momentum	$\rho \mathbf{u} \cdot \nabla \mathbf{u} = \nabla \cdot \left[-p\mathbf{I} + \frac{\mu}{\varepsilon}(\nabla \mathbf{u} + (\nabla \mathbf{u})^T) - \frac{2\mu}{3}(\nabla \cdot \mathbf{u})\mathbf{I} \right] + \rho \mathbf{g} - \frac{\mu}{K}\mathbf{u}$	(2)
Species	$\nabla \cdot \left[\rho w_j \mathbf{u} - \rho w_j \sum_{k=1}^{n} \tilde{D}_{jk} \left(\nabla x_k + (x_k - w_k)\frac{\nabla p}{p} \right) \right] = R_j$	(3)
Energy	$\nabla \cdot (-k\nabla T + \rho C_p T \mathrm{u} + \sum_j h_j \mathbf{N}_j) = Q$	(4)
Electronic Charge	$-\nabla \cdot (\sigma_e \nabla \phi_e) = i_{a/c}$	(5)
Ionic Charge	$-\nabla \cdot (\sigma_i \nabla \phi_i) = -i_{a/c}$	(6)

electrolyte and MIEC electrodes, whereas electronic charge equations are solved in the MIEC electrodes, while the current collectors are assumed to be infinitely conductive. Electronic current leaks are calculated via an explicit relationship and given as boundary conditions to the electronic charge equation at the cathode–electrolyte interface. Details of model development can be found in Serincan et al. [21]

2.1. Governing equations

The governing equations and the corresponding source terms can be found in Tables 2 and 3, respectively. The last term in the right hand side of Eq. (2) is the Darcy's term and it accounts for the additional pressure drop in the porous media. The momentum equation given by Eq. (2) is valid for the whole model domain, where

Table 3
Source terms.

Mass and Species	$R_j = \pm \frac{i_{a/c}}{nF} \mathrm{MW}_j$	(7)
Energy	$Q = (E_{max} - V_{cell}) i_a$	(8)
Anode transfer current	$i_a = A_a \exp\left(-\frac{EA_a}{RT}\right) \left(\frac{x_{H_2} p}{x_{H_2}^{ref} p_{ref}}\right)^{\gamma_{H_2}} \left(\frac{x_{H_2O} p}{x_{H_2O}^{ref} p_{ref}}\right)^{\gamma_{H_2O}} \sinh\left(\frac{\alpha_a F}{RT}\eta_a\right)$	(9)
Cathode transfer current	$i_c = A_c \exp\left(-\frac{EA_c}{RT}\right) \left(\frac{x_{O_2} p}{x_{O_2}^{ref} p_{ref}}\right)^{\gamma_{O_2}} \sinh\left(\frac{\alpha_c F}{2RT}\eta_c\right)$	(10)

the porosity, ε and the permeability, K is unity and infinity for the open channels, respectively.

Eq. (3) is the Maxwell–Stefan equation that solves the multicomponent species conservation. Maxwell–Stefan equations are solved for hydrogen and water in the anode and oxygen and water in the cathode, whereas nitrogen is treated as background species for both sides. The derivation of Eq. (3) and the calculation of Maxwell–Stefan diffusivities $\tilde{D}_{jk}$ based on binary diffusivities can be found in [24].

Differently form our previous model [21], binary diffusivities are calculated using Fuller's method [25,26]. Using $T^{1.75}$ temperature dependence, Fuller's method is shown to fit the experimental data more accurately than the kinetic theory at elevated temperatures, i.e. $T^{1.5}$ [27].

$$D_{jk} = \frac{0.00143T^{1.75}}{pM_{jk}^{1/2}\left(V_j^{1/3} + V_k^{1/3}\right)^2} \tag{11}$$

where p is pressure [bar], V_j is the special diffusion volumes of Fuller et al. [25], which are listed for SOFC gases in [28], and M_{jk} is the combined molecular weight which is calculated as $M_{jk} = 2[1/M_j + 1/M_k]^{-1}$. In the electrodes binary diffusion coefficients are further corrected to account for porosity and the tortuosity of the medium via the relation given by Zhu et al. [7]

$$D_{jk}^{\text{eff}} = \frac{\varepsilon}{\tau} D_{jk} \tag{12}$$

In this study, we also account for the Knudsen diffusion in the porous regions via the Dusty-Gas Model (DGM). The general formulation of DGM for a multicomponent mixture of n species is given by Mason and Malinauskas [29] as:

$$\sum_{\substack{j=1 \\ j\neq i}}^{n} \frac{x_j\mathbf{N}_i - x_i\mathbf{N}_j}{D_{ij}^{\text{eff}}} + \frac{\mathbf{N}_i}{D_{i,\text{Kn}}^{\text{eff}}} = -\frac{1}{RT}\nabla p_i \tag{13}$$

where $\mathbf{N}_i$ is the diffusive flux and x_i is the mole fraction of the ith species. Eq. (13) can be transformed into n-dimensional matrix notation as [30]

$$[B][\mathbf{N}] = -\frac{1}{RT}(\nabla p) \tag{14}$$

where B is a function of species mole fractions and binary diffusivities. Multiplying both sides with the inverse of B we have a relation for fluxes:

$$[\mathbf{N}] = -\frac{1}{RT}[B]^{-1}(\nabla p) \tag{15}$$

which is then used to replace the diffusive term in Eq. (3) in porous media.

In Eq. (13) $D_{i,\text{Kn}}^{\text{eff}}$ is the effective Knudsen diffusion coefficient which is calculated from Mason and Malinauskas [29] as

$$D_{i,\text{Kn}} = \frac{4}{3}\frac{\varepsilon}{\tau}\sqrt{\frac{8RT}{\pi M_i}}r_p \tag{16}$$

where r_p is the average pore radius. Significance of the Knudsen term in Eq. (13) depends on the average pore radius of the electrodes. For larger pores Knudsen diffusion coefficient becomes greater and Knudsen term gets smaller, therefore Knudsen diffusion can be neglected. However, for small pore sizes, Knudsen diffusion coefficient becomes comparable to binary diffusivities and Knudsen term should be included in the Maxwell–Stefan formulation to have a better representation of the species transport. In our case, at 550 °C effective Knudsen diffusion coefficient for H_2 is calculated as 5.616×10^{-5} m^2 s^{-1} for average pore radius of 0.5 μm whereas effective binary diffusion coefficient for H_2–N_2 pair is 2.53×10^{-4} m^2 s^{-1}.

The ionic conductivities of the electrolyte and electrode materials are obtained from the literature in the form of the Arrhenius relation. For GDC the data is taken from Xia and Liu [31] and for LSCF-GDC the data is taken from Wang et al. [32]. The ionic conductivities in S m^{-1} are calculated as

$$\sigma_{i,\text{GDC}} = \frac{6.991 \times 10^6 \exp(-0.64/(k_bT))}{T} \tag{17}$$

$$\sigma_{i,\text{GDC-LSCF}} = 3.388 \times 10^5 \exp\left(\frac{-0.90}{(k_bT)}\right) \tag{18}$$

Source terms in Eqs. (5) and (6) are the rate of charge transfer and are given by Eqs. (9) and (10) for anode and cathode, respectively.

At the cathode, electrolyte interface flux boundary condition for electronic charge conservation is used to implement electronic leakage currents which is given with the expression derived from [33].

$$-\mathbf{n}\cdot(\sigma_i\nabla\phi_i) = j_{\text{leak}};\quad j_{\text{leak}} = \frac{\phi_{\text{eq}} - \phi_{e,c}}{L}\sigma_{i,\text{elc}}\left(\frac{p_\theta}{p_{O_2,c}}\right)^{1/4} \times \frac{\exp((F/RT)\phi_{e,c}) - 1}{1 - \exp(-(F/RT)(\phi_{\text{eq}} - \phi_{e,c}))} \tag{19}$$

where p_θ, is the oxygen partial pressure when electronic conductivity is equal to the ionic conductivity in the electrolyte.

3. Numerical implementation

The model is implemented in the commercial multiphysics software, COMSOL 3.4, which uses finite element method to discretize the partial differential equations. With the COMSOL's flexibility of choosing different types of elements in the same geometry, our 2D axisymmetric model consists of 3799 triangular and 1940 quadrilateral mesh elements. Analyses are carried out with the built-in parametric solver utilizing PARDISO as the linear system solver which is developed for the multiprocessing architectures [34]. COMSOL's parametric solver is used to generate the polarization curves for a specific set of operating conditions as the cell voltage is the input. Running the software on a workstation equipped with a quad-core X5355 INTEL XEON processor and 8 Gb of RAM, the simulations take around 10 min for a full polarization scan from 1.0 to 0.2 V with a step size of 0.025 V.

4. Results

The model is utilized to investigate the effects of operational parameters such as temperature, flow rate, fuel composition and pressure of the gas chambers. With the chosen parameters as listed in Table 4, the model is fitted with the performance data at different temperatures made available by Suzuki et al. [22].

Table 4
Fitting parameters.

Parameter	Value	Unit
$EA_a = EA_c$	95×10^3	kJ kmol^{-1}
A_a	3e16	A m^{-3}
A_c	3e14	A m^{-3}
$\alpha_a = \alpha_c$	0.5	
γH_2	1.25	
γH_2O	0.25	
γO_2	0.25	

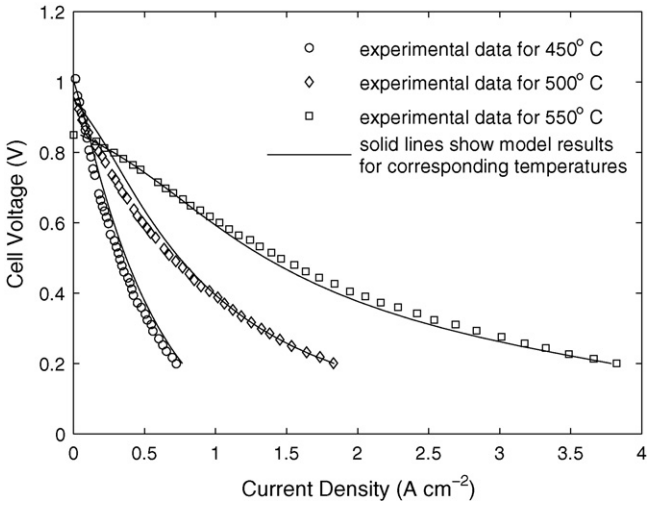

Fig. 2. Comparison of the polarization curves. Solid lines are the model results at different temperatures, lines with markers are the experimental results.

4.1. Effect of temperature and experimental validation

The model results are compared with the experimental results of Suzuki et al. [22] for three different temperatures, 450, 500 and 550 °C, respectively. As seen in Fig. 2, a good match is obtained between the simulation results and the experimental data. The model is capable of covering the OCV drops due to internal current leaks caused by electronic conduction through the electrolyte. Current leakage through the electrolyte is more dominant at higher temperatures.

At higher temperatures an increase in fuel cell performance is observed as properties such as activation energies, diffusivities and ionic conductivities enhance with increasing temperature. The most significant effects of the operating temperature are on the kinetics of the reaction and the ionic conductivity of the electrolyte. At higher temperatures, the kinetics of the reaction is faster and more current is generated.

Another effect is the increase of the ionic conductivities at higher temperatures which is explained by the Arrhenius type relation in Eqs. (17) and (18). Data of Xia and Liu [31] for the electrolyte material GDC shows values of the ionic conductivity as 0.335, 0.609, 1.025 S m^{-1} for 450, 500 and 550 °C, respectively.

Performance of the cell also increases due to the increased diffusion coefficients of the gases with temperature as described by Eq. (11). With increased diffusivity, hydrogen molecules reach reaction sites faster. Hence, a decrease in the mass transport losses enhances the performance of the cell. As previously discussed, diffusivity is correlated to temperature with $D \sim T^{1.75}$. However at lower temperatures, it is reported by Todd and Young [26] that this dependence decreases to $D \sim T^{1.5}$ as calculated from kinetic theory. Based on this discussion, it is expected that the decrease in mass transfer losses with a certain increase in temperature is more notable in a high temperature fuel cell than a low temperature fuel cell.

As current density increases, ohmic heating becomes more significant. Since for the same operating voltage SOFC generates more current at higher temperatures, ohmic heating is expected to be greater as well. Fig. 3 shows the increase in cell temperatures for three different inlet fuel temperatures. A temperature rise of about 29, 64 and 120 °C is predicted for inlet gas temperature of 450, 500 and 550 °C, respectively. This effect is reflected on performance such that the slope of the polarization curve decreases more at elevated temperatures.

Further, in Fig. 3, it is seen that the temperature contours are distorted toward the flow direction in the fuel channel whereas in the air channel a symmetrical distribution is predicted. This can be explained as the fuel is supplied to the anode chamber at a total flow rate of 25 ccm at 550 °C whereas the cathode uses the ambient stagnant air. At this flow rate, fuel passing through a channel with a radius of 4 mm results in very large velocities which induces a significant convective heat transfer from the cell to the anode chamber. On the other hand, at the cathode side heat is transferred from the cell to the air chamber mainly by conduction, as natural convection has a negligible effect on the temperature distribution. As a result more uniform temperature distribution is predicted. Moreover, as seen more clearly in Fig. 3c, radial flow is induced right after the flow diffuses out of the anode tube. Consequently, the temperature contours are distorted outwards radially.

Another important discussion on the effects of temperature are on the internal current leaks. As reported in Ref. [35] as well as predicted in our previous study [21], the electronic current leaks through the electrolyte due to the reduction of GDC are more significant at higher temperatures. Fig. 4 shows the ionic current density profiles at the anode-electrolyte interface for different operating temperatures at a fixed operating current density of 0.53 A cm^{-2}. Operating current density is calculated as the difference between the ionic current and the electronic leakage currents. The average ionic current density is found to be around 0.65 A cm^{-2} for 550 °C.

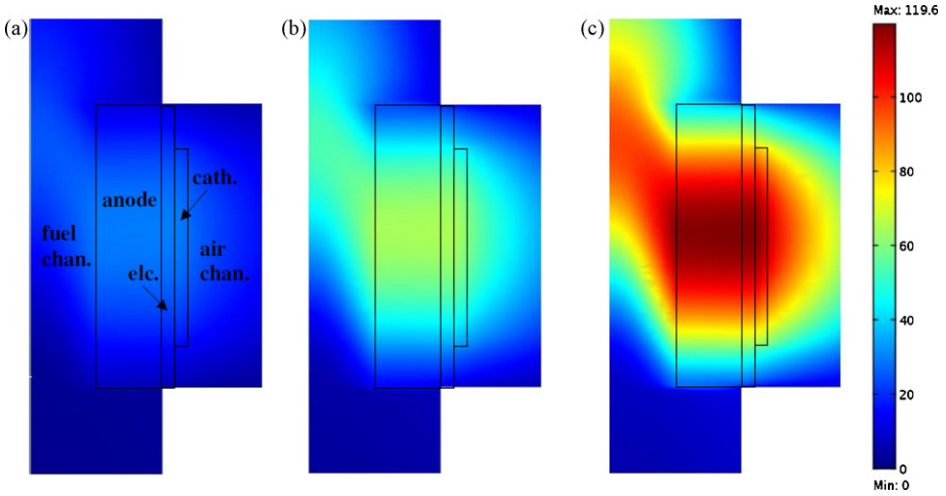

Fig. 3. Temperature difference between inlet and the cell for inlet fuel temperatures of (a) 450 °C, (b) 500 °C, (c) 550 °C.

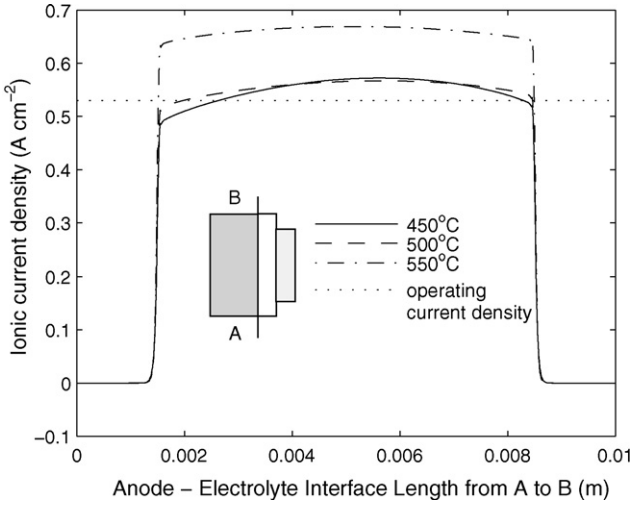

Fig. 4. Ionic current density profiles along the anode–electrolyte interface as a function of inlet fuel temperature at a fixed operating current density of 0.53 A cm^{-2}. Insert shows where the profiles are drawn in the anode–electrolyte–cathode assembly. Dotted line shows the operating current density and it is drawn for comparison purposes.

A fuel cell providing an output current density of 0.53 A cm^{-2} will have a loss of 0.12 A cm^{-2} due to the electron leak through the electrolyte. On the other hand at 450 °C and 500 °C the profiles are very similar and the average values are close to the operating current density. However, the magnitude of the ionic current density for 500 °C is a higher since more electron leaks are present.

Moreover conferring to these profiles it should be noted that the cathode is not coated all over the surface of the anode-electrolyte tube. The cathode is coated only for 0.7 cm on a 1 cm tube. So anode regions across which there is a lack of cathode coating are not able to generate any current. This is reflected in the profile as current density is predicted as zero for axial distance less than 0.15 cm and between 0.85 and 1 cm.

4.2. Effect of fuel flow rate

Flow rate is another important parameter in determining the fuel cell performance. Fig. 5 shows the polarization curves for different flow rates. In this step, fuel composition is kept constant and the effect of flow rate is investigated at 550 °C and 5 kPa anode back

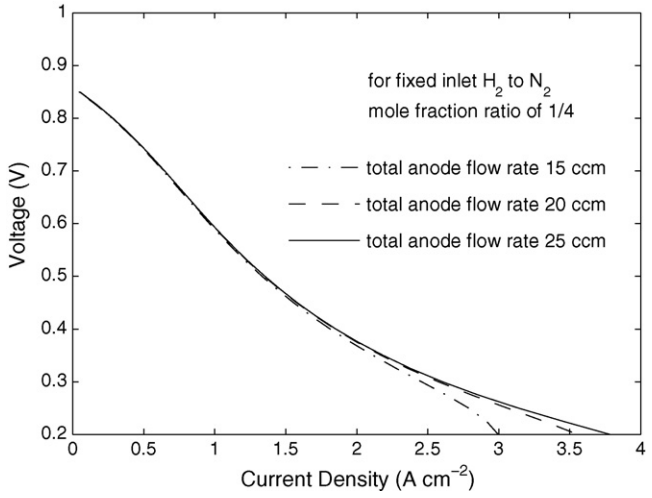

Fig. 5. Polarization curves for different anode flow rates at 550 °C and fixed H_2 to N_2 molar ratio of 1/4.

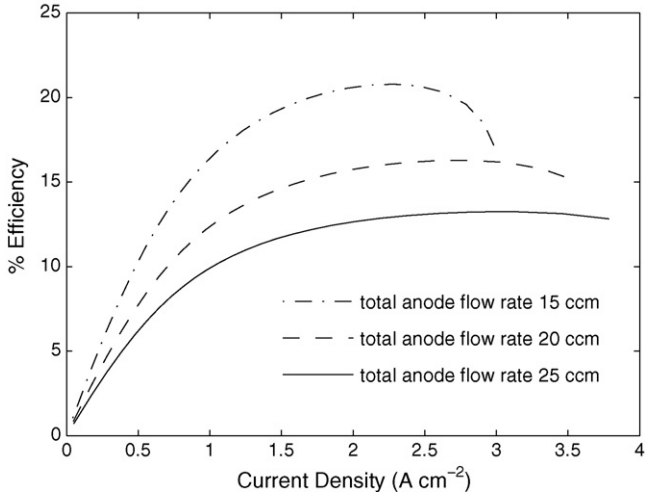

Fig. 6. Efficiency vs operating current density for different anode flow rates at 550 °C and fixed H_2 to N_2 molar ratio of 1/4.

pressure. Results show that high fuel flow rates increase the output power. This is due to the decrease in concentration overpotentials as more hydrogen is being supplied to the active reaction sites with increasing flow rate. The effect is seen more clearly in the high current density region where concentration overpotentials are more effective. At lower current densities, since there is a small amount of hydrogen used in the reaction; the ratio of hydrogen to the overall fuel mixture is equivalent for different flow rates therefore the polarization curves are identical. However, for lower flow rates the slopes of the polarization curves at higher current densities become steeper showing that mass transport limitations are more notable. With a change in the hydrogen flow rate from 3 to 5 ccm, maximum current density increased from 3.0 to 3.8 A cm^{-2}.

On the other hand, increase in flow rate contrarily affects the efficiency of the fuel cell operation. Fuel cell efficiency defined as,

$$\eta = \frac{i_{\text{op}} V}{i_{\text{ionic}} h_{\text{H}_2\text{O}}^{\text{for}}/(2F)} U \tag{20}$$

the ratio of the cell output power to the chemical energy of the fuel supplied. Fuel utilization is defined as the ratio of the reacted hydrogen to the amount of hydrogen available in the fuel stream.

$$U = \frac{\dot{m}_{\text{H}_2}^{\text{reac}}}{\dot{m}_{\text{H}_2}^{\text{in}}} \tag{21}$$

At the same current density, since the reacted hydrogen is also the same for each case, the fuel utilization is larger for lower flow rate values. At the same current density, 2 ccm more fuel is wasted for inlet hydrogen flow rate of 5 ccm compared to that of 3 ccm. This is directly reflected on the efficiency curves such that the fuel cell efficiency is lower for higher fuel flow rates, even when higher power density is generated.

Higher fuel flow rate is advantageous for lessening the mass transport losses, but there is a trade-off when fuel cell efficiency is concerned. For the optimum operation, flow rate should be selected carefully depending on the desired operating current density. If the cell is desired to be operated in the mid-range current densities, there is little need for supplying fuel at higher flow rates. Indeed if Figs. 5 and 6 are considered simultaneously, it can be suggested that up to 2.0 A cm^{-2}, it is better to run the cell at lower flow rates since there is a small difference between the polarization curves when the efficiency plots show huge discrepancy in the favor of lower flow rates. However, if current densities more than 2.0 A cm^{-2} are required, one may argue to interchange the supe-

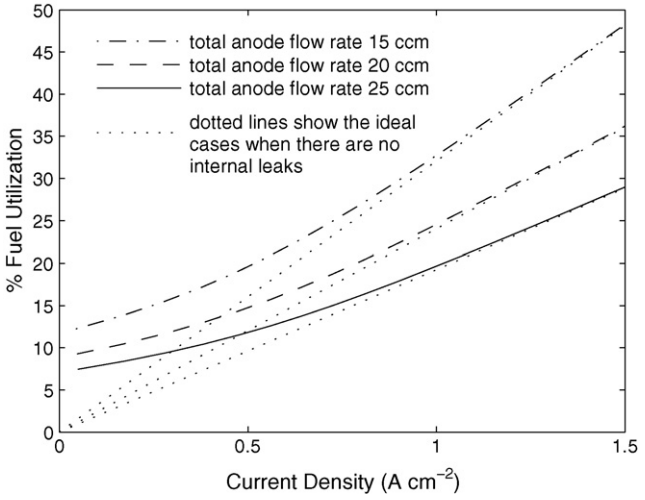

Fig. 7. Utilization vs operating current density up to 1.5 A cm^{-2} for different anode flow rates at 550 °C and fixed H_2 to N_2 molar ratio of 1/4. The dotted lines represent the ideal cases when there are no internal current leaks.

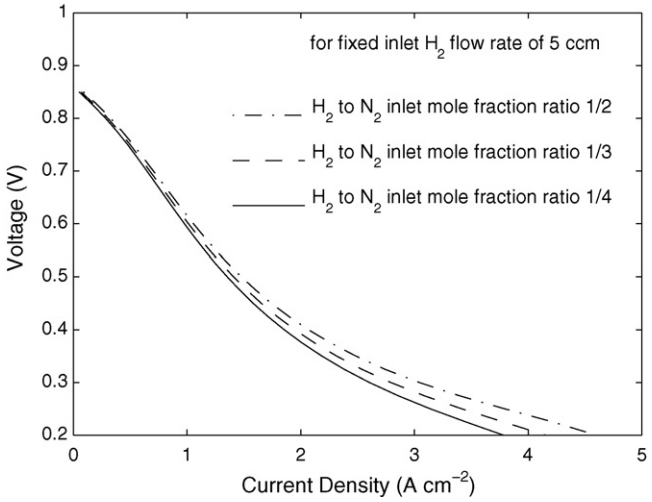

Fig. 8. Polarization curves for different fuel compositions at 550 °C and fixed inlet H_2 flow rate of 5 ccm.

riority of the efficiency with higher power density since after this point the difference in polarization curves looks more notable as the gap between the efficiency curves get narrower. In this case higher flow rates may be preferred. Indeed, if extensive current densities are desired such as those beyond 3 A cm^{-2} the cell has to run on high flow rates as the mass transport limitations are significant enough to hinder cell operation at these regions. It should be noted that these discussions do not include a fuel recirculation system due to small size. In case of fuel recirculation, the trade-off is between the increased power density and the parasitic losses for fuel recirculation rather than the fuel wasted.

Fig. 7 shows the fuel utilization curves, as described in Eq. (20), as a function of flow rate up to 1.5 A cm^{-2}. It should be noted that, the utilization is not zero when the current density is zero. The current density shown in Fig. 7 is cell operating current density and it differs from the ionic current density due to the internal electronic current leak. Although hydrogen is consumed and fuel cell reaction occurs under open circuit conditions (i.e. zero external current), all the electronic charge is transferred through the electrolyte. For 15 ccm total flow rate, the cell does not generate significant external current even when 12% of the hydrogen in the fuel stream is reacted. Hence in the region up to 1 A cm^{-2} where the effect of internal current leaks is significant, the utilization curves are not linear.

4.3. Effect of fuel composition

To analyze the effect of fuel composition on cell performance, nitrogen flow rate is changed when hydrogen flow rate is kept constant along with the other operating conditions. The experimental data is based on fuel composition of 5 ccm H_2 and 20 ccm N_2. Two more cases are considered for N_2 flow rate of 15 and 10 ccm when H_2 flow rate is kept at 5 ccm. These three cases correspond to H_2 to N_2 inlet mole fraction ratios of 1/4, 1/3, 1/2, respectively. In Fig. 8, it is shown that as the hydrogen mole ratio increases, fuel cell performance improves. This is related to the mass transport efficiency when there is relatively more hydrogen in the fuel stream than nitrogen. It is predicted that by increasing the ratio from 1/4 to 1/2, maximum current density increases from 3.8 to 4.5 A cm^{-2} at 0.2 V.

Fig. 9 shows the hydrogen mole fractions along the anode–electrolyte interface at 0.2 V and 550 °C as a function of fuel composition. Based on the discussion in Fig. 4, recall that anode reaction takes place in a certain region, i.e. from 1.5 mm above the anode inlet up to 1.5 mm below the anode outlet due to shorter cathode coating. This is reflected in the mole fraction profiles similarly. In Fig. 9, the corresponding regions can be distinguished by the changes in the shape of each profile. In the active region the slope of the profile is steeper for higher mole fractions; consumption rate of H_2 is greater. As a result of this, at the outlet of the anode tube, the H_2 mole fraction becomes smaller although the inlet mole fractions are greater.

4.4. Effect of anode pressure

The anode side pressure is another important operation parameter affecting the cell performance. Back pressure is applied on the anode as 5, 50 and 100 kPa (gauge) and the overall effects are shown in Fig. 10. It is observed that the higher the back pressure is, the more power is generated from the cell. There are two competing effects of pressure on the fuel cell operation. The first one is related to the effect of pressure on gas diffusivity. Gas diffusivity decreases with an increase in gas pressure as described in Eq. (11). However, total gas concentration increases with pressure, e.g. through ideal

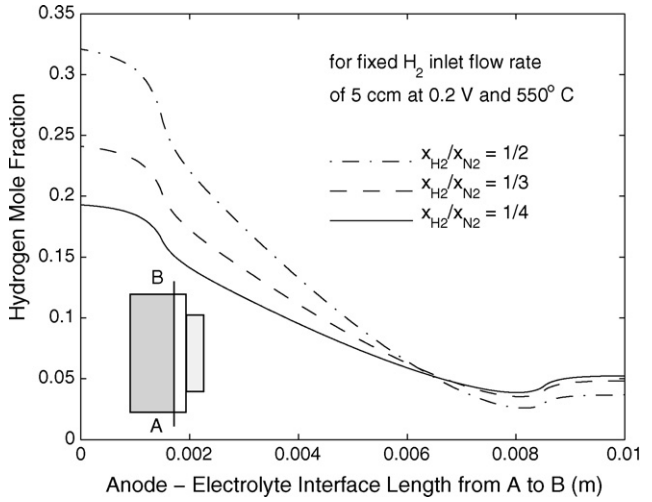

Fig. 9. Hydrogen mole fraction profiles along the anode–electrolyte interface as a function of inlet fuel composition. Insert shows where the profiles are drawn in the anode–electrolyte–cathode assembly.

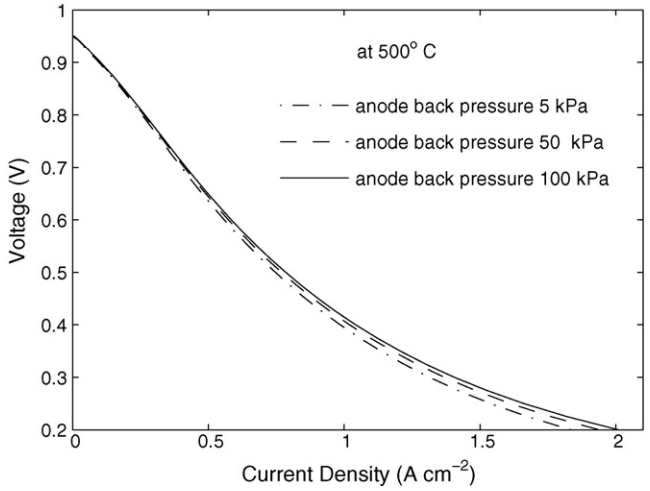

Fig. 10. Polarization curves for different anode back pressures at 500 °C and fixed inlet H_2 to N_2 ratio of 1/4 at a total flow rate of 25 ccm.

gas law: $c = p/R_uT$, and the second effect is related to that as the reaction rate is a function of species concentration. An increase in anode back pressure boosts the reaction rate according to Eq. (9). This overwhelms the adverse effect of pressure and the overall cell performance enhances with the increase in anode back pressure. For example, for a back pressure increase of 100 kPa, the current density increased from 1.83 to 2.05 A cm^{-2} at 0.2 V.

4.5. Effect of cathode pressure

As it is seen in Fig. 11, an increase in air pressure increases the output power of the cell similar to the effects of anode pressure. However there are two main differences observed when Fig. 11 is compared with Fig. 10. First, it is observed that the same amount of increase in cathode pressure results in a greater increase in current density. Secondly, when the cathode side pressure increases from 50 to 100 kPa, the increase in current density is smaller than when the pressure is changed from 0 to 50 kPa. However, with the same increments on the anode side pressure, closer performance increase is predicted.

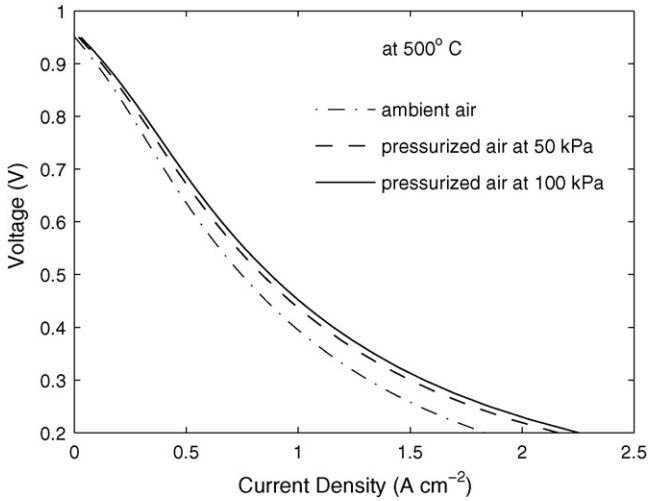

Fig. 11. Polarization curves for different air pressures at 500 °C and fixed inlet H_2 to N_2 ratio of 1/4 at a total flow rate of 25 ccm.

The first phenomenon can be explained by discussing the Nernst equation, e.g.:

$$\phi^{c}_{eq} - \phi^{a}_{eq} = \frac{-\Delta G^{\circ}(T)}{2F} + \frac{RT}{2F} \ln\left(\frac{p_{H_2} p_{O_2}^{0.5}}{p_{H_2O}}\right) \quad (22)$$

Considering the pressure term (inside the natural logarithm), when the pressure of the anode chamber increases, a change is not expected in the fuel cell equilibrium voltage since hydrogen partial pressure is in the numerator and water partial pressure is in the denominator. On the other hand, an increase in oxygen partial pressure is directly reflected on the resulting equilibrium voltage.

Cell performance being more sensitive to a change in cathode pressure is related to the different reaction kinetics on each side. The cathode reaction is slower than that of the anode and the changes in cathode has a greater influence on the overall reaction. Thus, an improvement in cathode reaction kinetics influences the output current density more significantly. This also explains second difference between Figs. 10 and 11. By increasing air pressure, cathode reaction kinetics become more comparable to that of anode, i.e. faster, and further increase in air pressure will have a smaller effect on the overall cell performance, since anode kinetics may determine the overall performance.

5. Conclusions

A computational fluid dynamics based SOFC model is developed to perform parametric analyses for a micro-tubular SOFC. Effects of temperature, fuel flow rate, fuel composition, anode pressure and cathode pressure on fuel cell performance are investigated. We have shown that increase in temperature results in better cell performance due to the increase in catalytic activity, ionic conductivity and decrease in mass transport losses. We have also shown that at higher operating temperatures the internal current leaks associated with the electron transfer through the electrolyte are more significant. It is predicted that if the output current demand is 0.53 A cm^{-2}, the fuel cell has to generate ionic current density of 0.65 A cm^{-2} at 550 °C as at this condition the leakage currents sum up to 0.12 A cm^{-2}. Moreover, it is concluded that the fuel flow rate should be chosen according to the desired operating range such as; at mid-range current densities lower flow rate is suggested because of the efficiency of the cell, and in the higher current density range, higher flow rate should be chosen (i.e. a stoichiometric flow control) because of the output power implications. When fuel composition is considered, higher hydrogen content is favorable for power output, efficiency and thermal management. Increases in anode side and cathode side pressures have two distinct effects on cell performance: increase in pressure reduces reactant diffusivity but increases catalytic activity. However, the latter overwhelms the adverse effect of decreased mass transport and cell performance is always observed to improve with larger back pressure. When the effects of pressure on the anode and cathode sides are compared, it is seen that fuel cell performance is more sensitive to changes in the air pressure mainly due to the slow reaction kinetics of the cathode.

Acknowledgements

This work was supported by New Energy and Industrial Technology Development Organization (NEDO) of Japan, as part of the Advanced Ceramic Reactor Project, and the School of Engineering at the University of Connecticut.

References

[1] N.Q. Minh, T. Takahashi, Science and Technology of Ceramic Fuel Cells, Elsevier, Amsterdam, 1995.
[2] S. Livermore, J. Cotton, R. Ormerod, J. Power Sources 86 (2000) 411–416.
[3] V. Dorer, R. Weber, A. Weber, Energy Build 37 (2005) 1132–1146.
[4] A. Hawkes, P. Aguiar, C.A. Hernandez-Aramburo, M. Leach, N.P. Brandon, T.C. Green, et al., J Power Sources 156 (2006) 321–333.
[5] K. Alanne, A. Saari, I.V. Ugursal, J. Good, J Power Sources 158 (2006) 403–416.
[6] P. Costamagna, P. Costa, V. Antonucci, Electrochim. Acta 43 (1998) 375–394.
[7] H. Zhu, R.J. Kee, V.M. Janardhanan, O. Deutschmann, D.G. Goodwin, J. Electrochem. Soc. 152 (2005) A2427.
[8] S. Campanari, P. Iora, Fuel Cells 5 (2005) 34–51.
[9] V.M. Janardhanan, O. Deutschmann, J. Power Sources 162 (2006) 1192–1202.
[10] M. Ni, M.K.H. Leung, D.Y.C. Leung, Fuel Cells 7 (2007) 269–278.
[11] M. Ni, M.K.H. Leung, D.Y.C. Leung, J. Power Sources 168 (2007) 369–378.
[12] M. Ni, M.K.H. Leung, D.Y.C. Leung, Energy Conv. Man. 48 (2007) 1525–1535.
[13] W. Jiang, R.X. Fang, J.A. Khan, R.A. Douga, J. Power Sources 162 (2006) 316–326.
[14] A. Abbaspour, K. Nandakumar, J.L. Luo, K.T. Chuang, J. Power Sources 161 (2006) 965–970.
[15] Y. Ji, K. Yuan, J.N. Chung, Y.C. Chen, J. Power Sources 161 (2006) 380–391.
[16] P. Lisbona, A. Corradetti, R. Bove, P. Lunghi, Electrochim. Acta 53 (2007) 1920–1930.
[17] C.O. Colpan, I. Dincer, F. Hamdullahpur, Int. J. Hydrogen Energy 32 (2007) 787–795.
[18] R. Bove, P. Lunghi, N.M. Sammes, Int. J. Hydrogen Energy 30 (2005) 189–200.
[19] W. Zhang, E. Croiset, P.L. Douglas, M.W. Fowler, E. Entchev, Energy Conv. Man. 46 (2005) 181–196.
[20] S. Campanari, J Power Sources 92 (2001) 26–34.
[21] M.F. Serincan, U. Pasaogullari, N.M. Sammes, J. Electrochem. Soc. 155 (2008) B1117–B1127.
[22] T. Suzuki, T. Yamaguchi, Y. Fujishiro, M. Awano, J. Electrochem. Soc. 153 (2006) A925–A928.
[23] B.C.H. Steele, Solid State Ionics 134 (2000) 3–20.
[24] C.F. Curtiss, R.B. Bird, Ind. Eng. Chem. Res. 38 (1999) 2515–2522.
[25] E.N. Fuller, P.D. Schettler, J.C. Giddings, Ind. Eng. Chem. 58 (1966) 19–27.
[26] B.E. Poling, J.M. Prausnitz, J.P. O'Conell, The Properties of Gases and Liquids (fifth ed), McGraw-Hill, New York, 2001.
[27] B. Todd, J.B. Young, J. Power Sources 110 (2002) 186–200.
[28] L. Andreassi, G. Rubeo, S. Ubertini, P. Lunghi, R. Bove, Int. J. Hydrogen Energy 32 (2007) 4559–4574.
[29] E.A. Mason, A.P. Malinauskas, Gas Transport in Porous Media: The Dusty-Gas Model, Elsevier, Amsterdam, 1983.
[30] R. Krishna, J.A. Wesselingh, Chem. Eng. Sci. 52 (1997) 861–911.
[31] C. Xia, M. Liu, Solid State Ionics 152–153 (2002) 423–430.
[32] S. Wang, T. Kato, S. Nagata, T. Honda, T. Kaneko, N. Iwashita, M. Dokiya, Solid State Ionics 146 (2002) 203–210.
[33] I. Riess, J. Electrochem. Soc. 128 (1981) 2077–2081.
[34] O. Schenk, K. Gärtner, W. Fichtner, A. Stricker, Future Gen. Comp. Sys. 18 (2001) 69–78.
[35] M. Gödickemeier, L.J. Gauckler, J. Electrochem. Soc. 145 (1998) 414–421.